

Constraining scalarization in scalar-Gauss-Bonnet gravity through binary pulsars

Victor I. Danchev^{1,*}, Daniela D. Doneva^{2,3,†} and Stoytcho S. Yazadjiev^{1,2,4‡}

¹*Department of Theoretical Physics, Faculty of Physics, Sofia University, Sofia 1164, Bulgaria*

²*Theoretical Astrophysics, Eberhard Karls University of Tübingen, Tübingen 72076, Germany*

³*INRNE – Bulgarian Academy of Sciences, 1784 Sofia, Bulgaria and*

⁴*Institute of Mathematics and Informatics, Bulgarian Academy of Sciences,
Acad. G. Bonchev Street 8, Sofia 1113, Bulgaria*

In the present paper we derive strong constraints on scalarization in scalar-Gauss-Bonnet (sGB) gravity using observations of pulsars in close binary systems. Since scalarized neutron stars carry a nonzero scalar charge, they emit scalar dipole radiation while inspiraling which speeds up the orbital decay. The observations support the conjecture that such radiation is either absent or very small for the observed binary pulsars. Using this, we determine the allowed range of parameters for sGB gravity. We also transfer the derived constraints to black holes in sGB gravity. It turns out that the maximum mass of a scalarized black hole can not exceed roughly five to ten solar masses, depending on the initial assumptions we make for the nuclear matter equations of state. The black hole scalar charge on the other hand can reach relatively large values that are potentially observable.

I. INTRODUCTION

The strong field regime of gravity is still a not well explored area that leaves a lot of freedom for modifications beyond general relativity (GR) [1]. Historically, one of the first observations that could constrain this regime were the pulsars in close binary systems [2–4]. More specifically, one can observe the shrinking of the orbit due to the emission of gravitational radiation. The observations show that this orbital decay fits very well the predictions of GR that constrained severely some theories of gravity predicting an additional channel of energy loss [5–9]. One prominent example in this context are the theories admitting scalarization and the scalar-tensor Damour-Esposito-Farese (DEF) model in particular. Such theories are characterized by field equations that are perturbatively equivalent to GR in the weak field regime while allowing for strong deviations from Einstein’s theory of gravity in the realm of large spacetime curvature. The presence of nonzero scalar charge of the neutron stars in the DEF model leads to the emission of scalar gravitational radiation that is an additional channel of energy loss and causes the binary system to inspiral faster compared to GR. Since this is not actually observed for pulsars in close binary systems, strong constraints were imposed on the DEF model [2, 5–7, 10]. Due to the extremely high accuracy of the pulsar timing observations it turns out that these constraints can not be easily improved by the observations of other gravitational wave sources such as binary neutron star mergers where indeed the gravitational wave signal from the inspiral is much stronger but the accuracy is far inferior [10, 11]. Thus the observations of pulsars in close binary systems still remain among the ultimate tools to test the strong field regime of gravity.

A class of alternative theories of gravity where scalarization was discovered a few years ago are the Gauss-Bonnet (GB) theories [12]. They are perhaps the most prominent subclass of quadratic theories of gravity defined by the addition of all possible geometrical invariants of second order to the theory action in addition to the classical Einstein-Hilbert term [13]. A strong motivation behind this type of modifications of Einstein’s theory comes from the attempts to quantize gravity. What makes Gauss-Bonnet theories special is the fact that the field equations are of second order lacking ghosts and they can be viewed also as a subclass of the Horndeski theories.

Compact objects in Gauss-Bonnet theories were first considered in the context of the so-called Einstein dilaton Gauss-Bonnet (EdGB) gravity where the coupling between the scalar field and the coupling is a linear function of the scalar field or an exponent of a linear function [14–23]. The studies showed that in this case the scalar charge and thus the scalar dipole radiation are either zero or negligible and hence the binary pulsar observations can not impose strong constraints on the theory [24]. This is not true, though, for classes of Gauss-Bonnet theories allowing for scalarization, that we will call scalar-Gauss-Bonnet (sGB) theories, for which the scalar charge can be large [25–27].

Even though scalarization in sGB gravity originally attracted a lot of attention in the context of black holes, it is possible to scalarize also neutron stars [26, 28, 29]. Thus one can impose constraints on the theory through binary pulsar observations which is the goal of the present paper. This is important because even though scalarization in sGB gravity brought a lot of excitement, little is known about the astrophysical implications. In particular, we constrain

* Electronic address: vidanchev@uni-sofia.bg

† Electronic address: daniela.doneva@uni-tuebingen.de

‡ Electronic address: yazad@phys.uni-sofia.bg

the possible range of values for the sGB gravity parameters through Markov Chain Monte-Carlo (MCMC) methods applied to the observation of the most suitable pulsar-white dwarf systems that are used also to constrain scalarization in the DEF model [7]. This has been performed by comparing the predicted effects due to scalar dipole radiation on the pulsar's period evolution (which is lacking for the pure GR case) with the observed period evolution of the star, considering the experimental measurement errors.

The paper is structured as follows. In Sec. II we briefly review the theory behind sGB gravity and building scalarized neutron star models in this theory. In Sec. III the methodology for constraining the theory through observations of pulsars in binary systems is described. The code setup and the results are discussed in Sec. IV. Sec. V is devoted to transferring these constraints to the black hole scalarization. The paper ends with Conclusions.

II. GRAVITATIONAL THEORY FORMULATION

We are working within the framework of sGB theory having the following action

$$S = \frac{1}{16\pi G_*} \int d^4x \sqrt{-g} [R - 2\nabla_\mu \varphi \nabla^\mu \varphi + \lambda^2 f(\varphi) \mathcal{R}_{GB}^2] + S_{\text{matter}}(g_{\mu\nu}, \chi), \quad (1)$$

where R is the Ricci scalar and ∇_μ is the covariant derivative, both with respect to the spacetime metric $g_{\mu\nu}$. The theory choice is made by setting the coupling function for the scalar field $f(\varphi)$ and the GB coupling constant λ which has the dimension of length. Lastly, the Gauss-Bonnet invariant is defined as $\mathcal{R}_{GB}^2 = R^2 - 4R_{\mu\nu}R^{\mu\nu} + R_{\mu\nu\alpha\beta}R^{\mu\nu\alpha\beta}$ with respect to the spacetime Ricci and Riemann tensors. The field equations corresponding to that action are

$$R_{\mu\nu} - \frac{1}{2}Rg_{\mu\nu} + \Gamma_{\mu\nu} = 2\nabla_\mu \varphi \nabla_\nu \varphi - g_{\mu\nu} \nabla_\alpha \varphi \nabla^\alpha \varphi + 8\pi G_* T_{\mu\nu}^{\text{matter}} \quad (2)$$

$$\nabla_\alpha \nabla^\alpha \varphi = -\frac{\lambda^2}{4} \frac{df(\varphi)}{d\varphi} \mathcal{R}_{GB}^2, \quad (3)$$

where $T_{\mu\nu}^{\text{matter}}$ is the matter energy-momentum tensor while $\Gamma_{\mu\nu}$ is defined as

$$\begin{aligned} \Gamma_{\mu\nu} = & -R(\nabla_\mu \Psi_\nu + \nabla_\nu \Psi_\mu) - 4\nabla^\alpha \Psi_\alpha (R_{\mu\nu} - \frac{1}{2}Rg_{\mu\nu}) + 4R_{\mu\alpha} \nabla^\alpha \Psi_\nu + 4R_{\nu\alpha} \nabla^\alpha \Psi_\mu \\ & - 4g_{\mu\nu} R^{\alpha\beta} \nabla_\alpha \Psi_\beta + 4R_{\mu\alpha\nu}^\beta \nabla^\alpha \Psi_\beta, \end{aligned} \quad (4)$$

and we have defined

$$\Psi_\mu = \lambda^2 \frac{df(\varphi)}{d\varphi} \nabla_\mu \varphi. \quad (5)$$

By applying the field equations to the contracted Bianchi identities, one can show that the matter energy-momentum tensor satisfies the conservation law

$$\nabla^\mu T_{\mu\nu}^{\text{matter}} = 0. \quad (6)$$

In the present paper we are studying static and spherically symmetric neutron stars in sGB gravity so the spacetime metric is given by the following ansatz

$$dS^2 = -e^{2\Phi(r)} dt^2 + e^{2\Lambda(r)} dr^2 + r^2(d\theta^2 + \sin^2\theta d\phi^2). \quad (7)$$

The matter source is taken as perfect fluid $T_{\mu\nu}^{\text{matter}} = (\rho + P)u_\mu u_\nu + Pg_{\mu\nu}$ where ρ , P and u^μ are respectively the energy density, pressure and the 4-velocity of the fluid. Lastly, we require the perfect fluid and the scalar field to respect the staticity and spherical symmetry of the spacetime which leads us to the following dimensionally reduced

field equations

$$\frac{2}{r} \left[1 + \frac{2}{r}(1 - 3e^{-2\Lambda})\Psi_r \right] \frac{d\Lambda}{dr} + \frac{(e^{2\Lambda} - 1)}{r^2} - \frac{4}{r^2}(1 - e^{-2\Lambda}) \frac{d\Psi_r}{dr} - \left(\frac{d\varphi}{dr} \right)^2 = 8\pi G_* \rho e^{2\Lambda}, \quad (8)$$

$$\frac{2}{r} \left[1 + \frac{2}{r}(1 - 3e^{-2\Lambda})\Psi_r \right] \frac{d\Phi}{dr} - \frac{(e^{2\Lambda} - 1)}{r^2} - \left(\frac{d\varphi}{dr} \right)^2 = 8\pi G_* P e^{2\Lambda}, \quad (9)$$

$$\begin{aligned} \frac{d^2\Phi}{dr^2} + \left(\frac{d\Phi}{dr} + \frac{1}{r} \right) \left(\frac{d\Phi}{dr} - \frac{d\Lambda}{dr} \right) + \frac{4e^{-2\Lambda}}{r} \left[3 \frac{d\Phi}{dr} \frac{d\Lambda}{dr} - \frac{d^2\Phi}{dr^2} - \left(\frac{d\Phi}{dr} \right)^2 \right] \Phi_r \\ - \frac{4e^{-2\Lambda}}{r} \frac{d\Phi}{dr} \frac{d\Psi_r}{dr} + \left(\frac{d\varphi}{dr} \right)^2 = 8\pi G_* P e^{2\Lambda}, \end{aligned} \quad (10)$$

$$\begin{aligned} \frac{d^2\varphi}{dr^2} + \left(\frac{d\Phi}{dr} - \frac{d\Lambda}{dr} + \frac{2}{r} \right) \frac{d\varphi}{dr} \\ - \frac{2\lambda^2}{r^2} \frac{df(\varphi)}{d\varphi} \left\{ (1 - e^{-2\Lambda}) \left[\frac{d^2\Phi}{dr^2} + \frac{d\Phi}{dr} \left(\frac{d\Phi}{dr} - \frac{d\Lambda}{dr} \right) \right] + 2e^{-2\Lambda} \frac{d\Phi}{dr} \frac{d\Lambda}{dr} \right\} = 0, \end{aligned} \quad (11)$$

where from eq. (5) we have

$$\Psi_r = \lambda^2 \frac{df(\varphi)}{d\varphi} \frac{d\varphi}{dr}. \quad (12)$$

Additionally, the hydrostatic equilibrium equation takes the form

$$\frac{dP}{dr} = -(\rho + P) \frac{d\Phi}{dr}, \quad (13)$$

which follows from (6) applied for a perfect fluid.

The regularity at the center and asymptotic flatness impose the following boundary conditions

$$\Lambda|_{r \rightarrow 0} \rightarrow 0, \quad \left. \frac{d\Phi}{dr} \right|_{r \rightarrow 0} \rightarrow 0, \quad \left. \frac{d\varphi}{dr} \right|_{r \rightarrow 0} \rightarrow 0. \quad (14)$$

and

$$\Lambda|_{r \rightarrow \infty} \rightarrow 0, \quad \Phi|_{r \rightarrow \infty} \rightarrow 0, \quad \varphi|_{r \rightarrow \infty} \rightarrow 0. \quad (15)$$

The leading order asymptotic of the scalar field at infinity has the form

$$\varphi \approx \frac{D}{r} + O(1/r^2). \quad (16)$$

where the scalar charge D is a constant directly related to the gravitational wave emission in close binary systems as we will discuss below.

The existence and stability of scalarized neutron star solutions has been studied by two of the present authors in [28]. In the present work we are solving equations (8)–(11) with the following commonly employed coupling function

$$f(\varphi) = \frac{\epsilon}{2\beta} [1 - \exp(-\beta\varphi^2)] \quad (17)$$

with $\beta > 0$ and $\epsilon = \pm 1$. While for both $\epsilon = \pm 1$ scalarized neutron stars solutions exist, only for positive ϵ static black holes can scalarize [25]. The minus sign of ϵ is associated with the so-called spin-induced scalarization [30–35] where development of scalar field is observed only for sufficiently fast rotating neutron stars. In order to obtain neutron star solutions for different β and λ values corresponding to one of the partners in a Neutron Star–White Dwarf (NS–WD) binary system we follow closely the methodology described in [28]. The rationale and constraints that can be imposed from observations of such systems are explored in the following section.

The coupling function choice (17) is by no means unique. Other couplings have also been used in the literature with the most prominent example being $f(\varphi) = \varphi^2$ [26] that matches (17) for very small scalar fields. Even though such quadratic coupling is the simplest one admitting scalarization, it leads to unstable scalarized black holes [36] and the behavior of the scalarized neutron star branches look also somewhat peculiar compared to the exponential coupling [29]. This can be cured (at least for black holes) with adding higher order φ terms in the coupling function [37, 38] or a self-interacting scalar field potential [39]. From a numerical point of view, though, the exponential coupling is

much more preferred when heavier simulations such as binary merger [40] or stellar core-collapse [41] are performed, as well as for rotating black hole solutions [34, 42]. Since our goal is not only to derive the constraints from binary pulsar experiments but also to apply them to constraints the properties of astrophysically relevant scalarized black hole, it is of great importance to work with a coupling function that leads to well behaved branches of solutions that is secured by the choice (17). Moreover, as the experience from other studies shows [43, 44], if we consider a modified coupling that still leads to well-behaved branches of solutions, the final results will remain qualitatively the same.

III. CONSTRAINTS FROM BINARY PULSARS OBSERVATION

As discussed in the introduction, the pulsars in close binary systems are a very useful tool to probe the strong field regime of gravity due to the possibility for a precise measurement of the orbital decay due to gravitational wave emission. We are focusing our investigation on a state-of-the-art observations of a set of three neutron star-white dwarf (NS-WD) binaries listed in Table I, following the MCMC strategy as formulated by [7], and derive constraints in the $\beta - \lambda$ space. These pairs are J0348+0432, J1012+5307 and J2222-0137, and the numerical values of the parameters for them are outlined in the table.

Quantity	J0348+0432 values	J1012+5307 values	J2222-0137 values
Orbital Period (P_b) in days	$0.102424062722 \pm 7 \times 10^{-12}$	$0.60467271355 \pm 3 \times 10^{-11}$	$2.44576454 \pm 18 \times 10^{-8}$
Eccentricity (e)	$2.6 \times 10^{-6} \pm 9 \times 10^{-7}$	$1.2 \times 10^{-6} \pm 3 \times 10^{-7}$	$3.8096 \times 10^{-4} \pm 4 \times 10^{-8}$
Intrinsic \dot{P}_b^{int} in (fs.s $^{-1}$)	-274 ± 45	-5 ± 9	-60 ± 90
NS to WD mass ratio $q \equiv m_p/m_c$	11.70 ± 0.13	10.5 ± 0.5	n/a
Pulsar mass m_p^{obs} in M_\odot	n/a	n/a	1.76 ± 0.06
Observed WD mass m_c^{obs} in M_\odot	$0.1715^{+0.0045}_{-0.0030}$	0.174 ± 0.007	1.293 ± 0.025

TABLE I: Physical parameters for the NS–WD pairs used for the inference of constraints. Values are obtained from [6, 45, 46] where the observed time derivatives are corrected using the Galactic potential of [47].

As a matter of fact initially we had considered more NS–WD binaries but based on the specifics of the problem, that has some important qualitative differences compared to the DEF model [7], we have kept only the three systems that impose the most stringent constraints with J0348+0432 being the most suitable one as discussed below. More specifically the remaining two NS–WD pairs from [7] have considerably lower pulsar masses of $1.47 M_\odot$ and $1.54 M_\odot$. As seen in [28], for greater λ the bifurcation point from the GR branch will appear at lower masses. Therefore, less massive neutron stars will generally provide constraints on λ starting from larger λ values and will not contribute to a distribution where constraints from more massive stars are considered. This will be seen in the numerical results for these three NS–WD pairs in IV B. The same methodology can be readily applied to future NS–WD pairs with higher pulsar mass but for the present time the system J0348+0432 offers the best constraints.

A posterior distribution of the parameters is obtained by integration over a set of distributions known as the prior, likelihood and model evidence based on Bayes’ theorem. Given a hypothesis \mathcal{H} (which is the sGB gravity for certain β and λ values in our case) and a data collection \mathcal{D} , the marginalized posterior distribution of the parameters is given by

$$P(\beta, \lambda | \mathcal{D}, \mathcal{H}, \mathcal{I}) = \int \frac{P(\mathcal{D} | \beta, \lambda, \Theta, \mathcal{H}, \mathcal{I}) P(\beta, \lambda, \Theta | \mathcal{H}, \mathcal{I})}{P(\mathcal{D} | \mathcal{H}, \mathcal{I})} d\Theta, \quad (18)$$

where \mathcal{I} is a collective notation for all prior background knowledge and Θ corresponds to all other unknown parameters except for (β, λ) . These are integrated over to obtain the marginalized posterior distribution in terms of just (β, λ) . Furthermore, in (18), $P(\beta, \lambda, \Theta | \mathcal{H}, \mathcal{I})$ is the prior on the full set of parameters (β, λ, Θ) , $P(\mathcal{D} | \beta, \lambda, \Theta, \mathcal{H}, \mathcal{I}) \equiv \mathcal{L}$ is the likelihood, while $P(\mathcal{D} | \mathcal{H}, \mathcal{I})$ is the model evidence. The choice of likelihood and prior distributions as well as the numerical implementation of the MCMC technique are discussed further down.

For a given NS–WD system, the gravitational dipole radiation can be described by 3 free parameters, namely the theory parameters (β, λ) and the central pressure P_c or central density ρ_c of the pulsar, provided that all other orbital details such as the eccentricity, orbital period, etc. are well measured. The central value of the scalar field φ_c on the other hand is obtained through a shooting method from the requirement that the scalar field is zero at infinity $\varphi_0 = 0$. In practice, for a given NS–WD system the central pressure is not known but can be solved for, given the system pulsar mass observation.

The MCMC runs evolve the 3 parameters through an affine-invariant ensemble sampler available with the Python `emcee` package [48, 49]. The prior distribution is homogeneously distributed in areas of the (β, λ) space where

scalarized solutions exist. The dimensionally reduced field equations are solved at each step with the imposed condition of matching the mass of a given pulsar from Table I. The likelihood function is then computed by comparing the observed decay of the binary system's orbital period with that predicted for the sGB theory with the given parameters from the simulations. Following [7], the logarithmic likelihood is defined as

$$\ln \mathcal{L} \propto -\frac{1}{2} \left[\left(\frac{\dot{P}_b^{\text{int}} - \dot{P}_b^{\text{th}}}{\sigma_{\dot{P}_b}^{\text{obs}}} \right)^2 + \left(\frac{m_p/m_c - q}{\sigma_q^{\text{obs}}} \right)^2 \right], \quad (19)$$

where m_p and m_c are the pulsar and companion masses of the system, q is the observed mass ratio, \dot{P}_b^{int} is the observed intrinsic orbital period decay rate, \dot{P}_b^{th} is the predicted one and σ_X^{obs} is the uncertainty from observations for the respective quantity X . The predicted orbital decay is dominated by the dipole scalar and quadrupole tensor radiation terms which are given by the following formulae [50, 51]

$$\dot{P}_b^{\text{dipole}} = -\frac{2\pi G_*}{c^3} g(e) \left(\frac{2\pi}{P_b} \right) \frac{m_p m_c}{m_p + m_c} D^2, \quad (20)$$

$$\dot{P}_b^{\text{quad}} = -\frac{192\pi G_*^{5/3}}{5c^5} f(e) \left(\frac{2\pi}{P_b} \right)^{5/3} \frac{m_p m_c}{(m_p + m_c)^{1/3}}, \quad (21)$$

where m_p and m_c are once again the masses of the pulsar and companion respectively, P_b is the orbital period of the binary system, D is the scalar charge of the neutron star and e is the eccentricity of the system. Therefore, for the purpose of the simulation, the period decay is evaluated as $\dot{P}_b^{\text{th}} = \dot{P}_b^{\text{dipole}} + \dot{P}_b^{\text{quad}}$. Lastly, the auxiliary functions of eccentricity $f(e)$ and $g(e)$ are given by

$$g(e) \equiv \left(1 + \frac{e^2}{2} \right) (1 - e^2)^{-5/2}, \quad (22)$$

$$f(e) \equiv \left(1 + \frac{73}{24}e^2 + \frac{37}{96}e^4 \right) (1 - e^2)^{-7/2}. \quad (23)$$

Note that the above methodology may also be applied to binary neutron stars (NS–NS pairs). Those have provided some of the most stringent constraints on modified gravitational theories but have generally been applied to representative EoSs [52–54]. It is significantly more difficult to distinct between the effects of EoS uncertainty and the theory parameters when NS–NS systems are concerned (with one or both NS potentially scalarized). The use of NS–WD pairs allows us to focus on the variation of parameters for only one of the partners in the system, while considering the WD parameters virtually known and thus constrain the theory parameters better [55, 56]. These specific pairs have been chosen based on the timing measurement accuracy and the masses. As will be shown further down – the more massive the NS in the pair is – the better constraints it can provide.

IV. CODE SETUP AND NUMERICAL RESULTS

All numerical simulations are performed with the coupling functions (17) having β as a dimensionless free parameter and for both signs of ϵ . All results are presented in terms of the dimensionless theory parameter defined as

$$\lambda \rightarrow \frac{\lambda}{R_0}, \quad (24)$$

where $R_0 \cong 1.4766$ km corresponds to half the Schwarzschild radius of a 1 solar mass object. For each integration of the reduced field equations, the boundary conditions (14) and (15) are imposed. Each star is solved as a shooting problem for the central values of φ_c and Φ_c determined by the asymptotics (15). The local mass can then be defined through Λ as $m = \frac{r}{2}(1 - e^{-2\Lambda})$ and at infinity m gives the total gravitational mass of the neutron star. The scalar charge of the neutron star is obtained from the leading term of the scalar field asymptotics (16). The numerical integration of (8)–(11) is performed through an adaptive step method based on the Dormand–Prince version [57] of the Runge-Kutta family implemented by the authors. As was already explored in [28], the shooting procedure is not always easy to converge and some manual work was required to choose appropriate initial guesses for the explored regions of (β, λ) . The complete flow of an MCMC run can be understood in terms of the following steps:

- Given the (β, λ) values and the pulsar mass m_p , a shooting method is performed to obtain the right central pressure P_c for a solution with this mass and the given theory parameters. The initial guess for P_c is taken to be the corresponding central value obtained from GR. Note that for two of the pulsars m_p is not directly known but derived from the ratio of the NS–WD masses $q \equiv m_p/m_c$.

- The GB neutron star solution is examined for consistency by checking that the asymptotic corresponds to the relationship (16). If so, the scalar charge is extracted.
- The dipole and quadrupole radiation terms are computed based on the obtained scalar charge through (20)-(21), the remaining quantities of the respective system are kept fixed based on the values for the respective NS-WD pair from Table I.
- The logarithmic likelihood is computed using eq. (19).
- The computed logarithmic likelihood and the uniform prior functions are passed to the `emcee` package function for evaluation of the posterior distribution and generation of new points.

For each of the runs, a total of 416000 points have been used for the `emcee` sampler in a parallel run. These do not include an initial "shakedown" run of 41600 points used to forget the initial conditions which have been originally chosen uniformly around the prior distribution range. The `emcee` sampler was run with 32 samplers, meaning that these points are split at 1300 shakedown and 13000 run points per random walker making use of parallel computation with the maximum available machine threads.

Since there are no clear limits to the theory parameters (β, λ) , different ranges were attempted in the early runs of the simulations. The range $\beta \in [400, 7000]$ was seen to provide good insight into the general behaviour of the relationship for $\epsilon = 1$. Solutions with $\beta > 6000$ lead to little or no differences between GR and the GB neutron stars. These branches tend to remain only very close to GR (to within a percent) and this is the reason why larger λ ranges are allowed for higher β values in all cases. On the other hand, for $\beta < 400$ it is computationally difficult to find solutions with realistic quadrupole values since these occur very close to the bifurcation point. As shown by the results presented further in Table III which will be discussed later, this is purely a numerical problem and it can be seen that the GB stars are present for arbitrarily small values of β , simply approaching the λ threshold. Both of these effects are clearly seen in the posterior distributions of the following section.

On the other hand, the λ range which provides physically meaningful solutions is highly dependent on the neutron star maximum mass and thus the EoS. For a given fixed neutron star mass m_p , decreasing λ for a particular EoS will lead to a critical point $\lambda_{\text{bif}}(m_p)$ for which the bifurcation point from the GR branch is exactly at that NS mass m_p . This value is also dependent on the EoS as we will see and is therefore an important parameter to know for each run since for $\lambda < \lambda_{\text{bif}}$ the scalarized GB branch does not yet exist and thus the scalar dipole radiation contribution is zero.

A. Interpretation and use of the results – standard scalarization with $\epsilon = 1$

The results of each MCMC run have been analyzed and visualized in two different ways: as contour and corner plots. The following Fig.1 is an example of these two visualizations for the same run of the MPA1 equation of state (EoS) with the J0348+0432 data and $\epsilon = 1$.

The contour plot shows 2D cross-sections of the posterior probability (in natural logarithm scale) as a function of the theory parameters. This plot is straightforward to understand as a distribution in the parameter space which is, however, normed only in the region of the prior distribution. This means that the results are not absolute in terms of probability but different values of the Z-axis are representative of relative probability with respect to each-other. These results cannot be taken directly as a probability, however, due to the lack of norm globally, but should only be considered in relative terms.

The corner plot on the other hand is a tool used in statistics and in particular MCMC to visualize projections of samples from higher-dimensional distributions. Unlike the contour plot, the corner plot is a density plot which indicates the number of samples which were drawn from the MCMC for the theory space of parameters. It does not represent a plot of probability but a scatter plot of where the samples are most dense. Due to the `emcee` affine-invariant ensemble sampler used, this density is related to the probability (and thus the qualitative likelihood between the two plots). The upper left and lower right sub-figures in the corner plot show the marginalized 1-d distributions with the 1-sigma levels shown as lines and contours in all 3 subplots. The Python `corner` package [58] has been used to generate the corner plots.

The corner plot gives some insight into the sampled data from the `emcee` package but the contour plot can be used for extracting the posterior distribution levels. In the case of a complete distribution, it would be most useful to extract different confidence intervals based on the cumulative distribution of all pulsars and EoS. In this case, however, we have no knowledge of the values below λ_{bif} for each specific pulsar and EoS. What is more, some pulsars and EoS combinations may provide λ constraints which are fully within the uncertainty zone ($\lambda < \lambda_{\text{bif}}$) of others. The most straightforward way to compare different constraints would be to compare where their bifurcation points occur

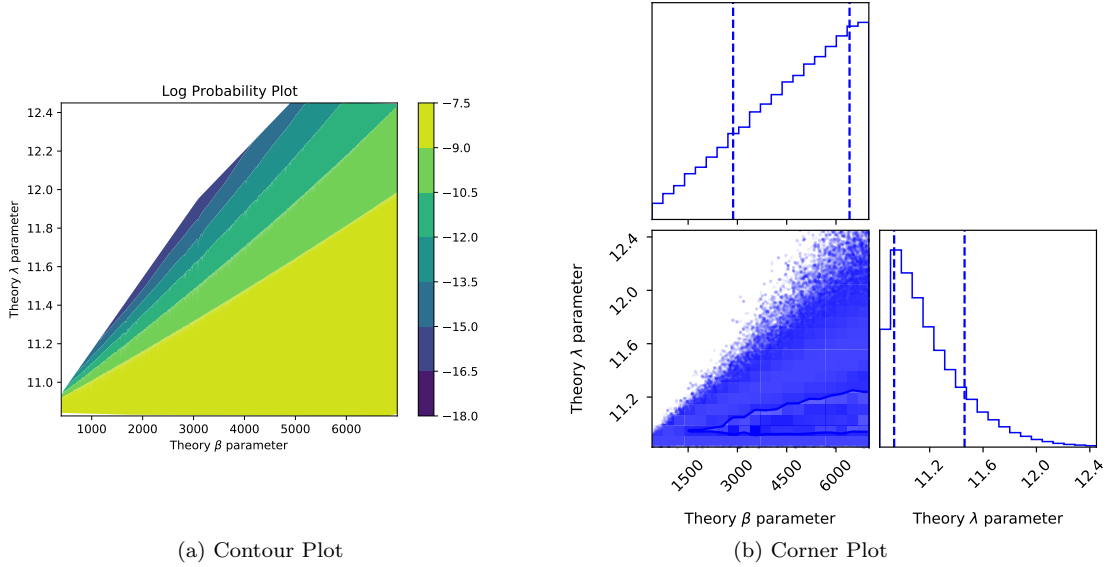


FIG. 1: Comparison of the contour and corner plots for the MPA1 EoS with the J0348+0432 NS-WD pair and $\epsilon = 1$.

NS-WD Pair \ Result	λ_{bif}	a_{-9}	b_{-9}
J0348+0432	10.82	1.64×10^{-4}	10.83
J1012+5307	12.32	7.94×10^{-5}	12.35
J2222-0137	12.88	1.53×10^{-3}	12.81

TABLE II: Results for the bifurcation line (λ_{bif}) and the boundary line at $\ln p = -9$ for the three pulsars with the MPA1 Equation of State.

as a lower threshold and use a posterior distribution “cutout” value as an effective upper bound on the constraint that can be generated by each EoS.

It is important to note that for all EoS and NS-WD pairs, the distributions are very similar. For all non-negligible values of the likelihood, the contour levels are always very well described by linear dependence of the kind

$$\lambda = a_{\ln p} \beta + b_{\ln p}, \quad (25)$$

where $a_{\ln p}$ and $b_{\ln p}$ are the two line parameters for a given posterior logarithmic probability $\ln p$ with base e . Moving towards lower $\ln p$ values, non-linear effects can be seen especially for the EoS with lower λ_{bif} values. One such example can be seen on Fig. 2 where the cut-off value between the posterior probability regions can no longer be well approximated by a linear dependence for $\ln p < -12$. The parameters of the linear fits (25) are chosen as representative for the constraints. Therefore, we have monitored the fit errors in order to ensure that in each case the fit of this form is well justified.

For all distributions, the cumulative probability for the region $\ln p < -9$ is most significant. Therefore, the line with a_{-9} and b_{-9} has been taken as a representative of the upper boundary for the posterior distribution. On the other hand, the natural lower boundary is the λ_{bif} below which we cannot use the distribution for any inference.

Table II summarizes the results for MPA1 with the three different pulsars for $\epsilon = 1$. It is sufficient to demonstrate that the most stringent constraints will arise from the most massive pulsar. That is why Table III provides data for the same parameters with different EoS and for J0348+0432. These are plotted and discussed further in the following two subsections.

Note that the value for $\ln p = -9$ is only used as an indicative probability cut-off and may be chosen in a different manner. This does not, however, change the end results qualitatively as it only affects the slope of the line from (25) within a small range. It is important to emphasize one condition for the comparison between the different linear fits to be consistent – the same area in the (λ, β) space must be used for the prior distributions. The reason for this is that the posterior is offset by a constant term proportional to the homogeneous distribution taken as prior (which depends only on the parameter space surface area). To show that such a cut-of is a consistent way to get constraints,

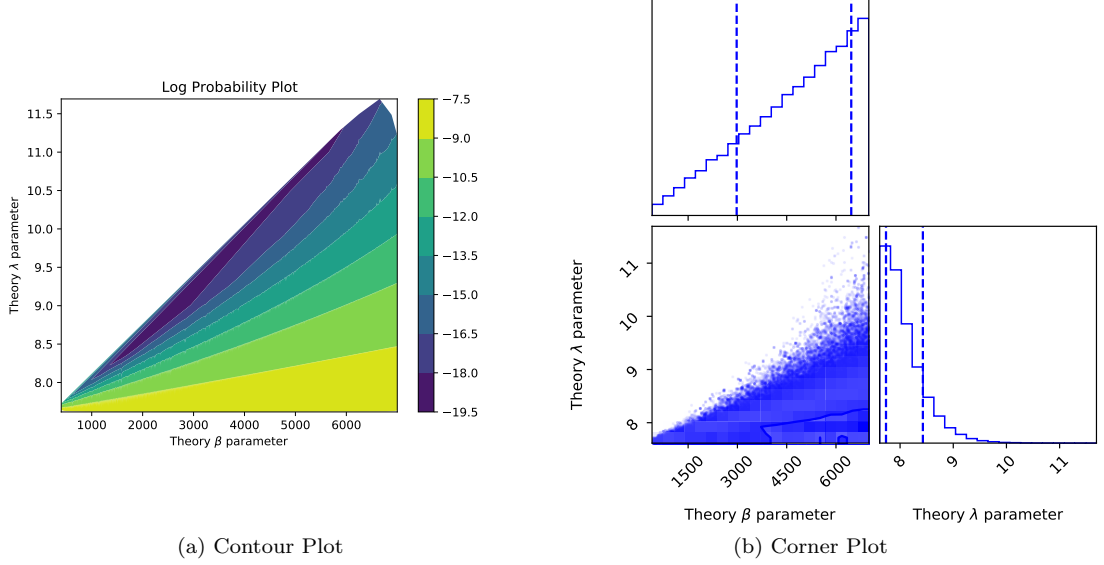


FIG. 2: Comparison of the contour and corner plots for the APR4 EoS with the J0348+0432 NS-WD pair and $\epsilon = 1$. The non-linear contour borders effect can be seen for $\ln p < -12$.

EoS \ Result	λ_{bif}	a_{-9}	b_{-9}
MS1	16.00	2.10×10^{-5}	16.02
MS1b	15.70	5.32×10^{-5}	15.77
MPA1	10.82	1.64×10^{-4}	10.83
APR3	9.57	1.38×10^{-4}	9.59
ENG	8.63	1.34×10^{-4}	8.73
H4	7.93	1.52×10^{-4}	7.98
APR4	7.56	1.23×10^{-4}	7.61
WFF2	7.32	1.16×10^{-4}	7.40
SLy	6.52	1.17×10^{-4}	6.58
WFF1	6.28	1.23×10^{-4}	6.35

TABLE III: Results for the bifurcation line (λ_{bif}) and the boundary line at $\ln p = -9$ for the 10 different EoS used with the J0348+0432 NS-WD pair and $\epsilon = 1$.

a visual comparison of the results with different cut-off values is performed in the figures of the following sections with 1-2 orders of magnitude (base e) difference. This does not lead to any qualitative differences in the results but only influences the slope of the lines minutely. As will be shown in the follow-up sections, these line slopes are generally of the same order for all EoS so the λ_{bif} is the decisive factor in terms of the constraints they can provide. For $\lambda < \lambda_{\text{bif}}$ no scalarized GB solutions exist for the given pulsar with mass m_p and thus this region is completely unrestricted by observational data for that pulsar.

B. Working with different NS-WD pairs – standard scalarization with $\epsilon = 1$

The following Fig. 3 shows the extracted boundaries for the MPA1 equation of state based on the above discussion for the NS-WD pairs from Table I. The two subplots show the results for two cut-off values of $\ln p$ which are -9 and -10.5 respectively (corresponding to two nearby contour borders on Fig.1). For each binary system the solid line is connected to the scalarization threshold and the dashed line comes from the probability distribution. The coloured region between these two lines is the one where scalarized neutron stars exist but their scalar radiation is within the observational bounds for this pulsar. In the region below the solid line scalarization for this pulsar mass is not

possible and thus it is also allowed by the observations of the corresponding binary system. We have decided not to color it for every pulsar, though, to avoid too many overlaps.

As it can be seen, the three double systems do not complement each-other in either case since the ranges of viable constraints are completely different. For example, J2222-0137 and J1012+5307 can provide constraints on the parameter space only for $\lambda > 12.9$ and $\lambda > 12.3$ respectively, while J0348+0432 puts those regions at a negligible probability relative to the region $\lambda < 12$, referencing the contour plot of Fig. 1.

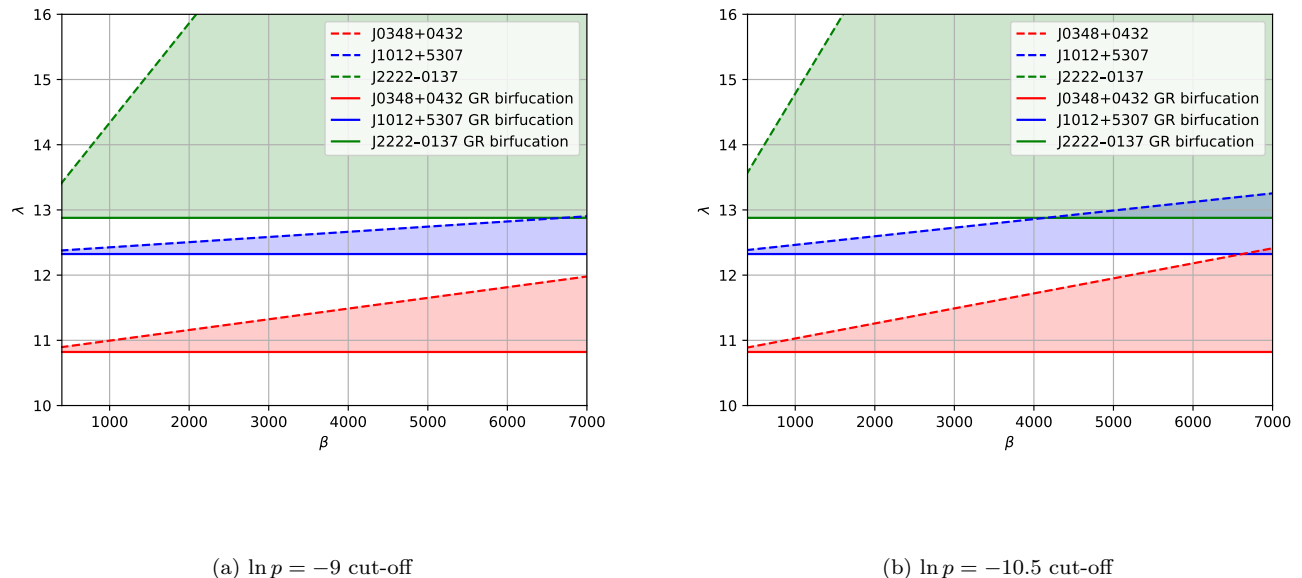


FIG. 3: Comparison of the bifurcation point λ_{bif} (solid line) and the posterior probability threshold (dashed lines) of $\ln p = -9$ (left panel) and $\ln p = -10.5$ (right panel) for the three pulsars listed in Table I and the MPA1 equation of state. The colored region between these two lines for each binary system is the one where scalarized neutron stars exist but their scalar radiation is within the observational bounds for this pulsar. The region below the solid line for each system has no constraints for the given NS-WD pair as it is below the bifurcation point, i.e. there is no scalarization for this pulsar mass and thus the scalar gravitational radiation is zero. Thus, even though this is also a region allowed by observation it has not been colored to avoid too many overlaps.

While lower values of $\ln p$ will definitely produce more overlap between the distributions, it is evident that even at a difference of a few orders of magnitude, this would not provide any qualitatively different constraints which could be used together. That is why in the following sections we have decided to stick to $\ln p = -9$ cut-off as a conservative and good enough choice.

The other two pulsars used in [7], that are J1738+0333 and J1909-3744, would produce even lower constraints. As shown in [28], the greater the λ value is, the lower the mass at which a bifurcation appears from the GR branch. Consider then that for a fixed EoS1, the bifurcation appears at $\lambda \cong \lambda_{\text{EoS1}}$ for J2222-0137 (which has $m_p = 1.76M_\odot$). Given another pulsar with $m_p < 1.76M_\odot$, it would certainly appear at a higher λ for the same EoS. Both J1738+0333 and J1909-3744 have a mass lower than $1.6M_\odot$, so they will certainly not lead to any further constraint as compared to the three systems considered. That is why we have not presented results for these two systems in the present paper.

In fact, Fig. 3 shows that the most stringent constraints from all NS-WD pairs will come from the most massive pulsar J0348+0432 and will not be further constrained even from the inclusion of the remaining two intermediate mass NS-WD binary in Table I. This is the rationale behind continuing only with the system which has the most massive pulsar J0348+0432 when computing constraints for multiple different EoS and transferring these constraints to black hole scalarization. We should note that an observation of a higher mass pulsar in the future will of course improve these constraints. Taking into account, though, that the present observations support the idea that the neutron star maximum mass is not much higher than two solar masses [59, 60], one can expect that this improvement will not be very large.

C. Constraints from different EoS – standard scalarization with $\epsilon = 1$

Having demonstrated that the most massive pulsar J0348+0432 gives the strongest constraints, let us turn now to the question how sensitive these constraints are to the nuclear matter EoS. The following Fig. 4 outlines the boundaries obtained at the bifurcation point $\lambda = \lambda_{\text{bif}}$ (solid line) and the posterior probability cut-off values $\ln p = -9$ and $\ln p = -11$ (dashed line) for eight different equations of state. Only data for the J0348+0432 system are displayed as it provides the most stringent constraints. We have used a diverse set of piecewise polytropic approximations of realistic nuclear matter EoS based on [61]. These include MPA1, APR3, APR4, ENG, H4, SLy, WFF1, WFF2. In our analysis we included also the MS1 and MS1b EoS that reach higher maximum mass but they provide very loose constraints with $\lambda_{\text{bif}} > 15$ and have been cut out of the figure for better visibility. The rest of the EoS in [61] have not been used due to their low maximum masses which do not support the existence of a pulsar such as that found in J0348+0432.

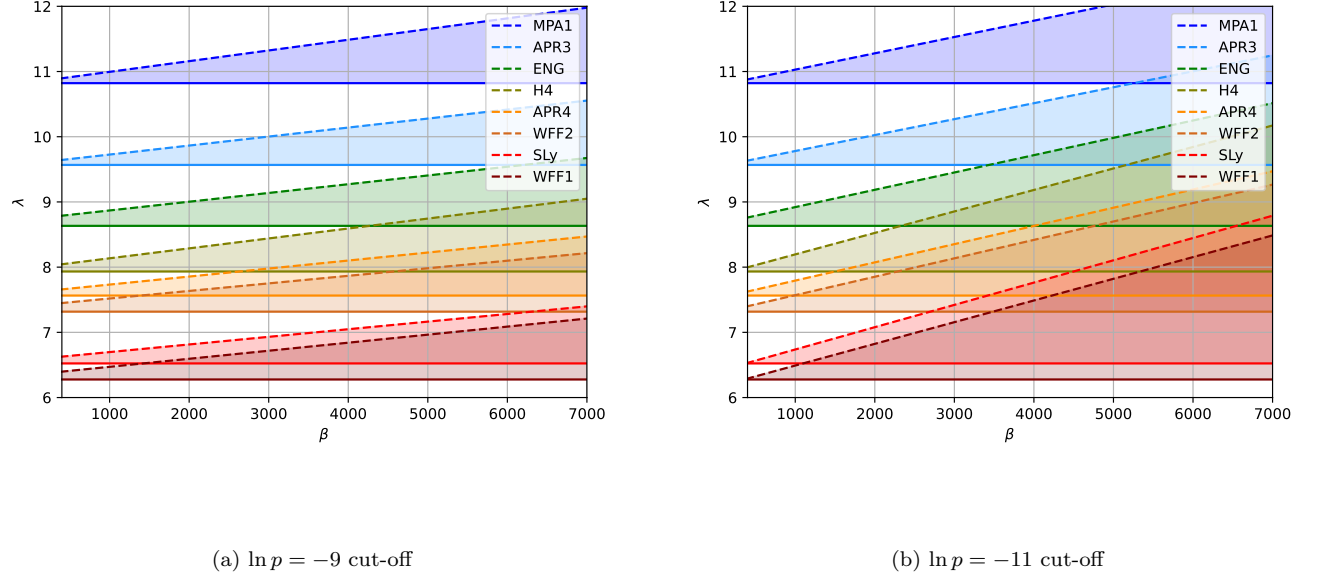


FIG. 4: Comparison of the bifurcation point λ_{bif} (solid line) and the posterior probability threshold of $\ln p = -9$ and $\ln p = -11$ (dashed lines) for J0348+0432 with eight realistic nuclear EoS. The colored region between these two lines for EoS is the one where scalarized neutron stars exist but their scalar radiation is within the observational bounds for this pulsar. The region below the solid line for each EoS has no constraints for the given NS-WD pair as it is below the bifurcation point, i.e. there scalarization for this pulsar mass is not possible and thus the scalar gravitational radiation is zero. Thus, even though this is also a region allowed by observation it has not been colored to avoid too many overlaps.

It is once again quite evident that except for a few EoS, the domains of mutual constraints are quite limited for both cut-off values. The most stringent limitations on the parameters come from SLy and WFF1 with the rest of the EoS providing virtually no additional constraint.

It is important to note that the slopes of all constraints are quite similar for all EOS (as can also be seen in Table III). It is therefore evident that the primary factor for the constraints on the (λ, β) space is when the bifurcation from GR occurs. The appearance of this bifurcation, however, has not been unambiguously traced to a EoS trait which can be quantified. The only observation we have made is that the higher maximum mass EOS, such as MPA1 and APR3 normally lead to weaker constraint. Taking into account the current EoS constraints [59, 60, 62], as well as the fact that a given EoS should reach the two solar mass barrier, one can safely claim that the constraints shown in Fig. 4 for the WFF1 EoS can not be significantly improved for another realistic EOS.

D. Constraining black hole scalarization with $\epsilon = 1$

Once we have derived and discussed in detail the constraints on the GB theory from binary pulsar observation, it will be interesting to apply them to constraint black hole scalarization. For fixed λ and β , though, a whole branch of scalarized black holes can exist spanning from the bifurcation point to zero black hole mass. We have decided to focus on two characteristics features of these branches. The first one is the black hole mass at the point of bifurcation that represents the maximum mass of a scalarized black holes and depends only on λ . The second one is the maximum scalar charge that can be reached for the whole sequence of scalarized solutions with fixed λ and β that is directly connected to the emitted scalar dipole radiation during black hole inspiral for example.

The following Fig. 5 shows the constraints from Fig. 4 overlaid on top of the maximum scalar charge and the maximum black hole mass for scalarized black holes in the sGB theory with corresponding (β, λ) value. We have displayed the constraints only for two EoSs, namely WFF1 and MS1, that represent the two limiting cases considered in the previous subsection with the strongest and the weakest constraint respectively.

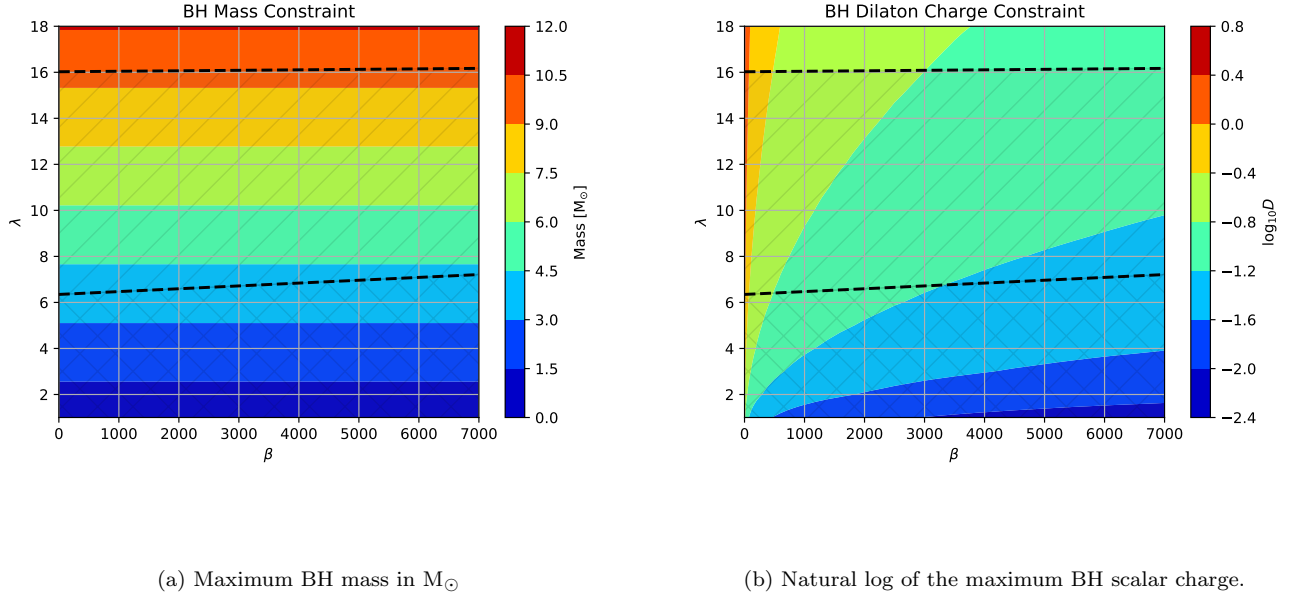


FIG. 5: Comparison of the lowest and highest constraints arising from the J0348+0432 and the considered EoS with cut-off logarithmic posterior value $\ln p = -9$. The shaded region with “x” pattern is where none of the EoSs provide any constraints on the parameters, i.e. scalarized neutron stars do not exist. The region marked with “/” is where at least one EoS provides some constraint on the parameters, i.e. scalarization exist for at least one of the considered EoS. The unmarked region is the one excluded from observations.

Let us focus first on the maximum mass of scalarized black holes depicted in the left panel of Fig. 5. This is the mass taken at the point of bifurcation and it does not depend on β but scales with λ [25, 43]. As one can see, the maximum mass that is still in agreement with binary pulsar observations is roughly $10M_\odot$ and this is for the relatively extreme MS1 EoS. If one takes a more conservative choice of an EoS that is in the preferred observational range [59, 60, 62], this constraints can easily drop to roughly $6M_\odot$. This practically excludes the possibility for scalarization for all binary black hole mergers observed until now through GW except for GW151226, GW170608 and GW190412. Thus, even if scalarized black holes in sGB gravity exist they can account only for a very small number of GW events. That is why constraining further sGB gravity with binary black hole merger observations will be a challenging task.

Even though the results for the maximum black hole mass do not look very optimistic, at least the scalar charge can reach relatively large values. As the results in [63, 64] show, such values of D can be tested also with EMRIs, assuming that the small orbiting object is a scalarized black hole. Still, the problem remains that for the vast majority of observed EMRIs, the orbiting black hole will have mass larger than the bounds discussed above.

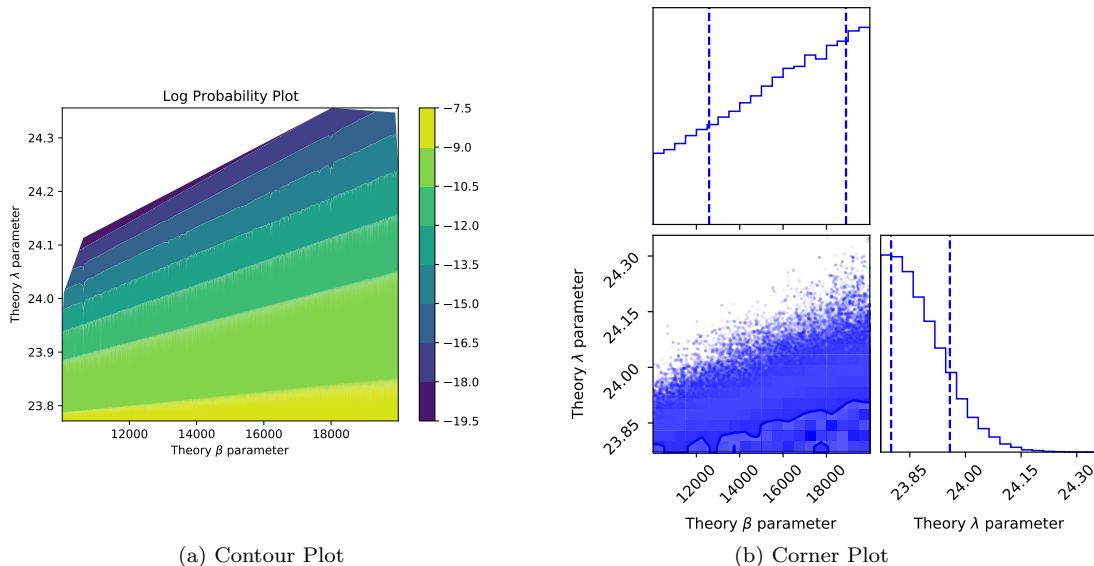


FIG. 6: Comparison of the contour and corner plots for the MPA1 EoS with the J0348+0432 NS-WD pair and negative $\epsilon = -1$.

E. Constraints with $\epsilon = -1$

Even though NS scalarization in sGB gravity is possible for both signs of ϵ , for $\epsilon = -1$ only rotating black holes can develop nontrivial scalar hair and a slightly different phenomenon is present which is the so-called spin-induced scalarization. The essence is that for rapidly rotating black holes the GB invariant can change sign close to the black hole horizon thus allowing for scalarization with opposite sign of the coupling function [30–35]. Therefore, it is important to obtain the constraints on the sGB gravity parameters also in the case of $\epsilon = -1$ that is the focus of this subsection. We will concentrate only on the NS-WD system J0348+0432 that can provide the strongest constraints for reasons described above.

The results of the MCMC run for $\epsilon = -1$ have been again analyzed and visualized in two different ways: as contour and corner plots. The results are presented in Fig.6 for the MPA1 equation of state (EoS) with the J0348+0432 data. As one can see the contour levels are very well described by linear dependence similar to the $\epsilon = 1$ case but it is apparent that the line slopes are much smaller. Fig. 7 on the other hand outlines the boundaries obtained at the bifurcation point $\lambda = \lambda_{\text{bif}}$ (solid line) and the posterior probability cut-off values $\ln p = -9$ and $\ln p = -11$ (dashed line) for the three most relevant equations of state again using only data for the J0348+0432 system that provides the most stringent constraints. As evident from the figure, the shaded region between the solid and the dotted line is very tiny, much smaller than the $\epsilon = 1$ case in Fig. 4. The reason for this lies into the fact that after the bifurcation point the neutron star solutions start developing scalar charge much more rapidly compared to the $\epsilon = 1$ case thus leading to strong scalar dipole radiation that is excluded from the observations. Therefore, in this case the observational constraint comes predominantly from the $\lambda = \lambda_{\text{bif}}$ line.

Here we will not transfer these constraints to black holes because of the complexity of finding rotating black hole solutions. In addition, we will have one more parameter – the black hole angular momentum, that makes imposing constraints of the type considered in the previous section, a formidable task. Thus we leave this for future studies.

Note that for $\epsilon = -1$ the numerical solutions are very difficult to find for lower values of β which is why a different interval has been used. As can be inferred from Table IV below, the values of λ_{bif} and b_{-9} are once again very similar (up to numerical error) demonstrating that the solutions continue down to $\beta = 0$ but become increasingly hard to differentiate from pure GR solutions.

V. CONCLUSIONS

Pulsars in close binary systems have proven over the years to give one of the most stringent constraints on strong field regime of gravity. The perfect fit of the pulsar’s orbit shrinking due to gravitational wave emission against the

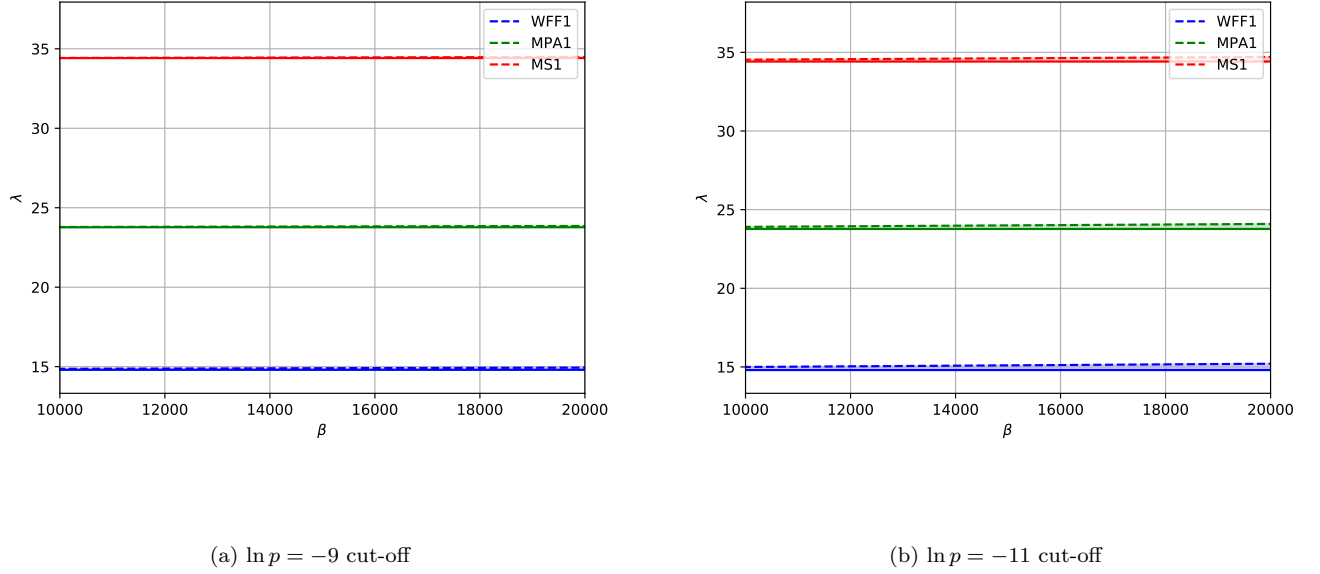


FIG. 7: Comparison of the bifurcation point λ_{bif} (solid line) and the posterior probability threshold of $\ln p = -9$ and $\ln p = -11$ (dashed lines) for J0348+0432 with three realistic nuclear EoS. The very tiny colored region between these two lines for each EoS is the one where scalarized neutron stars exist but their scalar radiation is within the observational bounds for this pulsar. The region below the solid line for each EoS has no constraints for the given NS-WD pair as it is below the bifurcation point, i.e. there scalarization for this pulsar mass is not possible and thus the scalar gravitational radiation is zero. Thus, even though this is also a region allowed by observation it has not been colored to avoid too many overlaps.

EoS \ Result	λ_{bif}	a_{-9}	b_{-9}
MS1	34.42	1.74×10^{-5}	34.36
MPA1	23.77	1.86×10^{-5}	23.72
WFF1	14.80	2.06×10^{-5}	14.79

TABLE IV: Results for the bifurcation line (λ_{bif}) and the boundary line at $\ln p = -9$ for the 3 representative EoS used with the J0348+0432 NS-WD pair and $\epsilon = 1$.

GR predictions has already put strong limits on a number of theories predicting an additional channel of energy loss such as scalar dipole radiation. In the present paper we have focused on a quite popular class of alternative theories of gravity that has not been studied yet in the context of binary pulsars, namely scalar-Gauss-Bonnet gravity admitting scalarization. The large interest in this theory comes from the fact that it offers an elegant way to produce black holes with scalar hair while leaving the weak field regime of gravity unaltered. Even though different astrophysical implications of such scalarized black holes were considered in the literature, the strong constraints coming from binary pulsar experiment have not been explored yet. Our goal was to fill this gap by considering a variety of observed double systems in the context of sGB gravity.

More specifically we have considered the three most suitable pairs of NS-WD binaries and examined the constraints these systems can impose on the theory parameters λ and β through Markov Chain Monte-Carlo (MCMC) methods applied to the observation. Here λ is the coupling constant between the Gauss-Bonnet invariant and the scalar field and β is a coefficient in the coupling function. We have considered both positive and negative signs of the coupling function. While neutron stars can scalarized independent of this sign, standard and spin-induced scalarization can be distinguished for black holes that leads to quite distinct properties of the hairy black holes.

For a given pulsar one can determine a minimum λ_{bif} below which scalarization is not possible (independent of

β) and thus for such values of the parameters the sGB theory is by definition in agreement with the binary pulsar observations. For $\lambda > \lambda_{\text{bif}}$, though, there is a range in the $\lambda - \beta$ plane where scalarization is allowed but the scalar dipole radiation is small enough so that the it is still within the observational uncertainty and is thus allowed by observations. We should point out, though, that this region with $\lambda > \lambda_{\text{bif}}$ is relatively narrow, especially for a negative sign of the coupling function (the sign that leads to spin-induced scalarization in the black hole case).

The results show that the more massive a pulsar is, the stronger the constraints on sGB gravity. In addition, these constraints are of course dependent on the nuclear matter EOS we employ but if we limit ourselves to modern realistic equations of state that are in agreement with the astrophysical observations, the spread is relatively small. With the discovery of new pulsars in close binary systems and the refinement of our knowledge of the high density equation of state, the constraints we derive in the present paper might of course be improved, but based on our results one can conclude that the expected improvement can be up to a few tens of percent. One should keep in mind that these results are for sGB gravity with massless scalar field. For a nonzero mass the scalar charge will be zero and the scalar gravitational radiation will be suppressed similar to the DEF model [65, 66] thus leading for agreement with binary pulsar observations for more or less arbitrary λ and β .

Having derived constraints on the sGB parameters λ and β , we have transferred them to static scalarized black holes in order to explore the possible range of astrophysically relevant solutions with scalar hair. We have focused on two characteristics of the scalarized black holes – the maximum mass a scalarized black hole can be achieved and the maximum scalar charge. We have obtained that the maximum mass of a static scalarized black hole is roughly $10M_{\odot}$ if we consider a broad set of equations of state, but drops to approximately $6M_{\odot}$ for equations of state that are in the preferred range according to astrophysical observations such as NICER and the binary neutron star mergers. Thus, it turns out that it is not that easy to observe a scalarized black hole because of the fact that it should have a relatively small mass and only a limited number of such objects are supposed to be observed in the near future. The maximum black hole scalar charge that is allowed by the binary pulsar observations is relatively large, though. Thus it can lead to clear observational signatures. These results were obtained for one form of the coupling function that is quite generic. Based on the experience in other related problems, we believe that the constraints on the black hole properties will not change considerably even if we modify the coupling while still allowing for scalarization. This is a study underway.

ACKNOWLEDGMENTS

VD, DD, and SY acknowledge the support by the National Science Fund of Bulgaria under Contract No. K-06-N-38/12. DD acknowledge financial support via an Emmy Noether Research Group funded by the German Research Foundation (DFG) under grant no. DO 1771/1-1. SY would like to thank the University of Tübingen for the financial support. Networking support by the COST actions CA15117 and CA16104 is gratefully acknowledged.

-
- [1] E. Berti *et al.*, Testing General Relativity with Present and Future Astrophysical Observations, *Class. Quant. Grav.* **32**, 243001 (2015), arXiv:1501.07274 [gr-qc].
 - [2] T. Damour and G. Esposito-Farese, Tensor - scalar gravity and binary pulsar experiments, *Phys. Rev. D* **54**, 1474 (1996), arXiv:gr-qc/9602056.
 - [3] N. Yunes and X. Siemens, Gravitational-Wave Tests of General Relativity with Ground-Based Detectors and Pulsar Timing-Arrays, *Living Rev. Rel.* **16**, 9 (2013), arXiv:1304.3473 [gr-qc].
 - [4] B. C. Seymour and K. Yagi, Testing General Relativity with Black Hole-Pulsar Binaries, *Phys. Rev. D* **98**, 124007 (2018), arXiv:1808.00080 [gr-qc].
 - [5] P. C. C. Freire, N. Wex, G. Esposito-Farèse, J. P. W. Verbiest, M. Bailes, B. A. Jacoby, M. Kramer, I. H. Stairs, J. Antoniadis, and G. H. Janssen, The relativistic pulsar-white dwarf binary PSR J1738+0333 II. The most stringent test of scalar-tensor gravity, *Mon. Not. Roy. Astron. Soc.* **423**, 3328 (2012), arXiv:1205.1450 [astro-ph.GA].
 - [6] J. Antoniadis *et al.*, A Massive Pulsar in a Compact Relativistic Binary, *Science* **340**, 6131 (2013), arXiv:1304.6875 [astro-ph.HE].
 - [7] L. Shao, N. Sennett, A. Buonanno, M. Kramer, and N. Wex, Constraining nonperturbative strong-field effects in scalar-tensor gravity by combining pulsar timing and laser-interferometer gravitational-wave detectors, *Phys. Rev. X* **7**, 041025 (2017), arXiv:1704.07561 [gr-qc].
 - [8] B. C. Seymour and K. Yagi, Probing massive scalar and vector fields with binary pulsars, *Phys. Rev. D* **102**, 104003 (2020), arXiv:2007.14881 [gr-qc].
 - [9] L. Shao, N. Wex, and S.-Y. Zhou, New Graviton Mass Bound from Binary Pulsars, *Phys. Rev. D* **102**, 024069 (2020), arXiv:2007.04531 [gr-qc].

- [10] T. Damour and G. Esposito-Farèse, Gravitational wave versus binary - pulsar tests of strong field gravity, *Phys. Rev. D* **58**, 042001 (1998), arXiv:gr-qc/9803031.
- [11] L. Sampson, N. Yunes, N. Cornish, M. Ponce, E. Barausse, A. Klein, C. Palenzuela, and L. Lehner, Projected Constraints on Scalarization with Gravitational Waves from Neutron Star Binaries, *Phys. Rev. D* **90**, 124091 (2014), arXiv:1407.7038 [gr-qc].
- [12] P. Kanti, N. E. Mavromatos, J. Rizos, K. Tamvakis, and E. Winstanley, Dilatonic black holes in higher curvature string gravity, *Phys. Rev. D* **54**, 5049 (1996), arXiv:hep-th/9511071.
- [13] K. S. Stelle, Renormalization of Higher Derivative Quantum Gravity, *Phys. Rev. D* **16**, 953 (1977).
- [14] S. Mignemi and N. R. Stewart, Charged black holes in effective string theory, *Phys. Rev. D* **47**, 5259 (1993), arXiv:hep-th/9212146.
- [15] N. Yunes and L. C. Stein, Non-Spinning Black Holes in Alternative Theories of Gravity, *Phys. Rev. D* **83**, 104002 (2011), arXiv:1101.2921 [gr-qc].
- [16] P. Pani, E. Berti, V. Cardoso, and J. Read, Compact stars in alternative theories of gravity. Einstein-Dilaton-Gauss-Bonnet gravity, *Phys. Rev. D* **84**, 104035 (2011), arXiv:1109.0928 [gr-qc].
- [17] P. Pani, C. F. B. Macedo, L. C. B. Crispino, and V. Cardoso, Slowly rotating black holes in alternative theories of gravity, *Phys. Rev. D* **84**, 087501 (2011), arXiv:1109.3996 [gr-qc].
- [18] T. P. Sotiriou and S.-Y. Zhou, Black hole hair in generalized scalar-tensor gravity, *Phys. Rev. Lett.* **112**, 251102 (2014), arXiv:1312.3622 [gr-qc].
- [19] T. P. Sotiriou and S.-Y. Zhou, Black hole hair in generalized scalar-tensor gravity: An explicit example, *Phys. Rev. D* **90**, 124063 (2014), arXiv:1408.1698 [gr-qc].
- [20] D. Ayzenberg and N. Yunes, Slowly-Rotating Black Holes in Einstein-Dilaton-Gauss-Bonnet Gravity: Quadratic Order in Spin Solutions, *Phys. Rev. D* **90**, 044066 (2014), [Erratum: *Phys. Rev. D* **91**, 069905 (2015)], arXiv:1405.2133 [gr-qc].
- [21] B. Kleihaus, J. Kunz, and E. Radu, Rotating Black Holes in Dilatonic Einstein-Gauss-Bonnet Theory, *Phys. Rev. Lett.* **106**, 151104 (2011), arXiv:1101.2868 [gr-qc].
- [22] B. Kleihaus, J. Kunz, and S. Mojica, Quadrupole Moments of Rapidly Rotating Compact Objects in Dilatonic Einstein-Gauss-Bonnet Theory, *Phys. Rev. D* **90**, 061501 (2014), arXiv:1407.6884 [gr-qc].
- [23] B. Kleihaus, J. Kunz, S. Mojica, and M. Zagermann, Rapidly Rotating Neutron Stars in Dilatonic Einstein-Gauss-Bonnet Theory, *Phys. Rev. D* **93**, 064077 (2016), arXiv:1601.05583 [gr-qc].
- [24] K. Yagi, L. C. Stein, and N. Yunes, Challenging the Presence of Scalar Charge and Dipolar Radiation in Binary Pulsars, *Phys. Rev. D* **93**, 024010 (2016), arXiv:1510.02152 [gr-qc].
- [25] D. D. Doneva and S. S. Yazadjiev, New Gauss-Bonnet Black Holes with Curvature-Induced Scalarization in Extended Scalar-Tensor Theories, *Phys. Rev. Lett.* **120**, 131103 (2018), arXiv:1711.01187 [gr-qc].
- [26] H. O. Silva, J. Sakstein, L. Gualtieri, T. P. Sotiriou, and E. Berti, Spontaneous scalarization of black holes and compact stars from a Gauss-Bonnet coupling, *Phys. Rev. Lett.* **120**, 131104 (2018), arXiv:1711.02080 [gr-qc].
- [27] G. Antoniou, A. Bakopoulos, and P. Kanti, Evasion of No-Hair Theorems and Novel Black-Hole Solutions in Gauss-Bonnet Theories, *Phys. Rev. Lett.* **120**, 131102 (2018), arXiv:1711.03390 [hep-th].
- [28] D. D. Doneva and S. S. Yazadjiev, Neutron star solutions with curvature induced scalarization in the extended Gauss-Bonnet scalar-tensor theories, *JCAP* **04**, 011, arXiv:1712.03715 [gr-qc].
- [29] R. Xu, Y. Gao, and L. Shao, Neutron stars in massive scalar-Gauss-Bonnet gravity: Spherical structure and time-independent perturbations, (2021), arXiv:2111.06561 [gr-qc].
- [30] A. Dima, E. Barausse, N. Franchini, and T. P. Sotiriou, Spin-induced black hole spontaneous scalarization, *Phys. Rev. Lett.* **125**, 231101 (2020), arXiv:2006.03095 [gr-qc].
- [31] S. Hod, Onset of spontaneous scalarization in spinning Gauss-Bonnet black holes, *Phys. Rev. D* **102**, 084060 (2020), arXiv:2006.09399 [gr-qc].
- [32] D. D. Doneva, L. G. Collodel, C. J. Krüger, and S. S. Yazadjiev, Black hole scalarization induced by the spin: 2+1 time evolution, *Phys. Rev. D* **102**, 104027 (2020), arXiv:2008.07391 [gr-qc].
- [33] E. Berti, L. G. Collodel, B. Kleihaus, and J. Kunz, Spin-induced black-hole scalarization in Einstein-scalar-Gauss-Bonnet theory, *Phys. Rev. Lett.* **126**, 011104 (2021), arXiv:2009.03905 [gr-qc].
- [34] C. A. R. Herdeiro, E. Radu, H. O. Silva, T. P. Sotiriou, and N. Yunes, Spin-induced scalarized black holes, *Phys. Rev. Lett.* **126**, 011103 (2021), arXiv:2009.03904 [gr-qc].
- [35] D. D. Doneva, L. G. Collodel, C. J. Krüger, and S. S. Yazadjiev, Spin-induced scalarization of Kerr black holes with a massive scalar field, *Eur. Phys. J. C* **80**, 1205 (2020), arXiv:2009.03774 [gr-qc].
- [36] J. L. Blázquez-Salcedo, D. D. Doneva, J. Kunz, and S. S. Yazadjiev, Radial perturbations of the scalarized Einstein-Gauss-Bonnet black holes, *Phys. Rev. D* **98**, 084011 (2018), arXiv:1805.05755 [gr-qc].
- [37] M. Minamitsuji and T. Ikeda, Scalarized black holes in the presence of the coupling to Gauss-Bonnet gravity, *Phys. Rev. D* **99**, 044017 (2019), arXiv:1812.03551 [gr-qc].
- [38] H. O. Silva, C. F. B. Macedo, T. P. Sotiriou, L. Gualtieri, J. Sakstein, and E. Berti, Stability of scalarized black hole solutions in scalar-Gauss-Bonnet gravity, *Phys. Rev. D* **99**, 064011 (2019), arXiv:1812.05590 [gr-qc].
- [39] C. F. B. Macedo, J. Sakstein, E. Berti, L. Gualtieri, H. O. Silva, and T. P. Sotiriou, Self-interactions and Spontaneous Black Hole Scalarization, *Phys. Rev. D* **99**, 104041 (2019), arXiv:1903.06784 [gr-qc].
- [40] J. L. Ripley and F. Pretorius, Dynamics of a \mathbb{Z}_2 symmetric EdGB gravity in spherical symmetry, *Class. Quant. Grav.* **37**, 155003 (2020), arXiv:2005.05417 [gr-qc].
- [41] H.-J. Kuan, D. D. Doneva, and S. S. Yazadjiev, Dynamical Formation of Scalarized Black Holes and Neutron Stars through Stellar Core Collapse, *Phys. Rev. Lett.* **127**, 161103 (2021), arXiv:2103.11999 [gr-qc].

- [42] P. V. P. Cunha, C. A. R. Herdeiro, and E. Radu, Spontaneously Scalarized Kerr Black Holes in Extended Scalar-Tensor–Gauss-Bonnet Gravity, *Phys. Rev. Lett.* **123**, 011101 (2019), arXiv:1904.09997 [gr-qc].
- [43] D. D. Doneva, S. Kiropelidi, P. G. Nedkova, E. Papantonopoulos, and S. S. Yazadjiev, Charged Gauss-Bonnet black holes with curvature induced scalarization in the extended scalar-tensor theories, *Phys. Rev. D* **98**, 104056 (2018), arXiv:1809.00844 [gr-qc].
- [44] W. E. East and J. L. Ripley, Dynamics of Spontaneous Black Hole Scalarization and Mergers in Einstein-Scalar-Gauss-Bonnet Gravity, *Phys. Rev. Lett.* **127**, 101102 (2021), arXiv:2105.08571 [gr-qc].
- [45] K. Lazaridis *et al.*, Generic tests of the existence of the gravitational dipole radiation and the variation of the gravitational constant, *Mon. Not. R. Astron. Soc.* **400**, 805 (2009), arXiv:0908.0285 [astro-ph.GA].
- [46] I. Cognard *et al.*, A Massive-born Neutron Star with a Massive White Dwarf Companion, *Astrophys. J.* **844**, 128 (2017), arXiv:1706.08060 [astro-ph.HE].
- [47] P. J. McMillan, The mass distribution and gravitational potential of the Milky Way, *MNRAS* **465**, 76 (2017).
- [48] J. Goodman and J. Weare, Ensemble samplers with affine invariance, *Communications in Applied Mathematics and Computational Science* **5**, 65 (2010).
- [49] D. Foreman-Mackey, D. W. Hogg, D. Lang, and J. Goodman, emcee: The MCMC Hammer, *Publ. Astron. Soc. Pac.* **125**, 306 (2013), arXiv:1202.3665 [astro-ph.IM].
- [50] T. Damour and G. Esposito-Farese, Tensor multiscalar theories of gravitation, *Class. Quant. Grav.* **9**, 2093 (1992).
- [51] P. C. Peters, Gravitational Radiation and the Motion of Two Point Masses, *Phys. Rev.* **136**, B1224 (1964).
- [52] T. Damour and G. Esposito-Farese, Tensor-scalar gravity and binary-pulsar experiments, *Phys. Rev. D* **54**, 1474 (1996).
- [53] N. Wex, Testing relativistic gravity with radio pulsars, (2014), arXiv:1402.5594 [gr-qc].
- [54] I. Cognard, P. C. C. Freire, L. Guillemot, G. Theureau, T. M. Tauris, N. Wex, E. Graikou, M. Kramer, B. Stappers, A. G. Lyne, and et al., A massive-born neutron star with a massive white dwarf companion, *The Astrophysical Journal* **844**, 128 (2017).
- [55] E. Berti, E. Barausse, V. Cardoso, L. Gualtieri, P. Pani, U. Sperhake, L. C. Stein, N. Wex, K. Yagi, T. Baker, and et al., Testing general relativity with present and future astrophysical observations, *Classical and Quantum Gravity* **32**, 243001 (2015).
- [56] M. Kramer, Pulsars as probes of gravity and fundamental physics, *International Journal of Modern Physics D* **25**, 1630029 (2016).
- [57] J. Dormand and P. Prince, A family of embedded runge-kutta formulae, *Journal of Computational and Applied Mathematics* **6**, 19 (1980).
- [58] D. Foreman-Mackey, corner.py: Scatterplot matrices in python, *Journal of Open Source Software* **1**, 24 (2016).
- [59] G. Raaijmakers *et al.*, Constraining the dense matter equation of state with joint analysis of NICER and LIGO/Virgo measurements, *Astrophys. J. Lett.* **893**, L21 (2020), arXiv:1912.11031 [astro-ph.HE].
- [60] G. Raaijmakers, S. K. Greif, K. Hebeler, T. Hinderer, S. Nisanke, A. Schwenk, T. E. Riley, A. L. Watts, J. M. Lattimer, and W. C. G. Ho, Constraints on the Dense Matter Equation of State and Neutron Star Properties from NICER’s Mass–Radius Estimate of PSR J0740+6620 and Multimessenger Observations, *Astrophys. J. Lett.* **918**, L29 (2021), arXiv:2105.06981 [astro-ph.HE].
- [61] J. S. Read, B. D. Lackey, B. J. Owen, and J. L. Friedman, Constraints on a phenomenologically parameterized neutron-star equation of state, *Phys. Rev. D* **79**, 124032 (2009), arXiv:0812.2163 [astro-ph].
- [62] F. Özel and P. Freire, Masses, Radii, and the Equation of State of Neutron Stars, *Ann. Rev. Astron. Astrophys.* **54**, 401 (2016), arXiv:1603.02698 [astro-ph.HE].
- [63] A. Maselli, N. Franchini, L. Gualtieri, and T. P. Sotiriou, Detecting scalar fields with Extreme Mass Ratio Inspirals, *Phys. Rev. Lett.* **125**, 141101 (2020), arXiv:2004.11895 [gr-qc].
- [64] A. Maselli, N. Franchini, L. Gualtieri, T. P. Sotiriou, S. Barsanti, and P. Pani, Detecting new fundamental fields with LISA, (2021), arXiv:2106.11325 [gr-qc].
- [65] F. M. Ramazanoğlu and F. Pretorius, Spontaneous Scalarization with Massive Fields, *Phys. Rev. D* **93**, 064005 (2016), arXiv:1601.07475 [gr-qc].
- [66] S. S. Yazadjiev, D. D. Doneva, and D. Popchev, Slowly rotating neutron stars in scalar-tensor theories with a massive scalar field, *Phys. Rev. D* **93**, 084038 (2016), arXiv:1602.04766 [gr-qc].